



# Dynamic Circuit-Based Unified Power Regulation for Hybrid AC/DC/DS Microgrids: A Comprehensive Approach to Static and Transient Control

Pengfeng Lin<sup>ID</sup>, Member, IEEE, Qingzuo Meng<sup>ID</sup>, Student Member, IEEE,  
Miao Zhu<sup>ID</sup>, Senior Member, IEEE, Amer M. Y. M. Ghias<sup>ID</sup>, Senior Member, IEEE,  
and Frede Blaabjerg<sup>ID</sup>, Fellow, IEEE

**Abstract**—Power regulation in hybrid ac/dc microgrids (MGs) is a critical concern, both in static and transient states. Static power regulation involves optimizing the dispatch of distributed energy resources (DERs) to meet the global load in proportion to their capacities, while transient power regulation requires each DER to manage load fluctuations based on their respective inertia during transients. However, the existing literature typically addresses these regulations separately focusing on static control often leads to the oversight of transient performance, and vice versa. To bridge this gap, this article introduces a unified modeling framework that integrates both static and transient power regulation, providing a comprehensive, full time-scale control strategy for hybrid systems. This approach visualizes the power regulation process through a dynamic equivalent circuit model, where power flow is represented as current variables on respective circuit elements. Furthermore, distributed energy storage systems are deployed centrally forming a distributed storage (DS) subgrid so that DS can be uniformly managed and participate in full time-scale regulation within the hybrid ac/dc/DS MG. The proposed unified model is validated through simulation and experiments, demonstrating its feasibility and effectiveness in achieving seamless static and transient power regulation.

**Index Terms**—Equivalent circuit models, hybrid ac/dc/DS microgrid, hybrid energy storage system (HESS), inertia regulation.

Received 20 November 2024; revised 24 March 2025 and 18 May 2025; accepted 25 June 2025. This work was supported in part by the National Natural Science Foundation of China under Grant U2166216 and in part by Shanghai Pujiang Talent Program under Grant 23PJ1405300. (Corresponding author: Miao Zhu.)

Pengfeng Lin, Qingzuo Meng, and Miao Zhu are with Shanghai Jiao Tong University, Shanghai 200240, China (e-mail: pengfeng\_lin@sjtu.edu.cn; rexxxx@sjtu.edu.cn; miao.zhu@sjtu.edu.cn).

Amer M. Y. M. Ghias is with Nanyang Technological University, Singapore 639798 (e-mail: amer.ghias@ntu.edu.sg).

Frede Blaabjerg is with Aalborg University, 9220 Aalborg, Denmark (e-mail: fbl@energy.aau.dk).

Digital Object Identifier 10.1109/TIE.2025.3585029

## I. INTRODUCTION

**H**YBRID ac/dc microgrids (MGs) offer a transformative solution to mitigate challenges associated with distributed energy resources (DERs) and advance grid decarbonization efforts. A hybrid ac/dc microgrid consists of four main components: dc subgrid, ac subgrid, power converter interfaces, and interlinking converters (ILCs). Power converters serve as the interfaces between DERs and MGs, while ILC bridges ac and dc subgrids to facilitate global power interaction across the system. The hybrid architecture offers several key advantages: 1) it enhances the overall system efficiency by directly connecting dc and ac sources/loads to their respective subgrids, eliminating unnecessary power conversion stages; 2) it provides a cost-effective turnkey solution by reducing investment costs; and 3) it enables more flexible power dispatch, largely driven by the high controllability of ILCs [1], [2].

However, the integration of dc and ac subgrids significantly increases system complexity, particularly in terms of static and transient power regulation. Static power regulation typically refers to the proportionate generation of power by DERs based on their capacities [3]. Transient power regulation ensures that during dynamic processes, DERs with higher inertia buffer more of power demand, while those with lower power density release power more gradually [4]. For instance, [5] describes the design of an ILC power control loop based on droop characteristics of both ac and dc grids to distribute global load demand according to each subgrid's capacity. In a more advanced configuration, multiple ILCs can be linked in parallel to form an ILC community within the hybrid ac/dc MG, as explored in [6]. This setup enables seamless power sharing across ILCs, helping to prevent power congestion between subgrids. A decentralized economic power-sharing strategy is also presented in [7], which proposes an incremental cost-based droop to reduce global operating costs during steady-state conditions.

Recent interest in transient power regulation in hybrid ac/dc MGs stems from the role of system inertia management in dynamic response. As discussed in [8], power-electronics-based systems often experience reduced overall inertia, leading to more severe deviations in dc voltage and ac frequency during

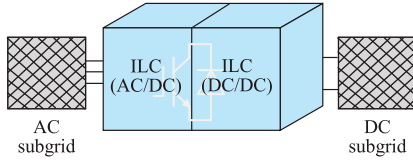


**Fig. 1.** Typical architecture of hybrid ac/dc MGs.

load changes. Without proper control, these deviations can cause sensitive loads or conventional generators to disconnect, potentially disrupting the system. To address this, [9], [10] propose virtual synchronous generator (VSG) control to improve frequency response in ac MGs, while [11] investigate virtual capacitor (VC) control to enhance dc bus inertia. Furthermore, [12] demonstrates how ILCs can coordinate transient power responses between ac and dc subgrids, enabling bidirectional virtual inertia support. Similarly, in [13], DERs within the global hybrid system preferentially direct power to subgrids with lower inertia during sudden load changes.

While static power regulation aims to equalize the normalized power output of DERs in steady-state, transient power regulation requires that power bursts from DERs are proportional to their inertia. However, the existing literature tends to address static and transient power regulation separately. Static power control studies often overlook transient performance, and those focused on transient power management neglect accurate static power sharing across the entire MG.

Fig. 1 illustrates the typical architecture of a hybrid ac/dc microgrid. As described in [14], [15], [16], energy storage systems (ESSs) are typically distributed within both ac and dc subgrids. Nevertheless, this practice brings higher unit storage capacity cost and operational cost than centralized energy storage [17]. In addition, ESS distributed in dc and ac MGs presents challenges in terms of capacity expansion. Distributed deployment will inevitably bring additional issues for placement space and different line impedances between ESSs and microgrid buses, which is further discussed in Section II-C. To overcome these limitations, a hybrid ac/dc/DS MG architecture is proposed, wherein distributed storage (DS) systems are integrated at an intermediate dc link of a two-stage ILC. It is mentioned that the control strategies in [14], [15], [16] primarily address static power management, while transient power regulation mechanisms remain under-explored. Moreover, these strategies fail to account for the coexistence of multiple ESSs with varying dynamic responses, which may shorten the lifespan of the storage systems due to indiscriminate control.

In response to these challenges, this article proposes a unified static and transient power regulation modeling approach, offering insights into a comprehensive power control scheme for ac/dc/DS MGs. Unlike conventional hybrid ac/dc/DS MG configurations, this article suggests utilizing a hybrid energy storage system (HESS) as the DS component. Through integral droop (ID) and traditional droop control, HESS components are managed based on their response speeds: slower ramp-rate storage systems handle low-frequency power demand, while the high-power-density storage systems address high-frequency power demand. By treating HESS as a whole, its transfer function from output power to DS bus voltage mirrors that of a simple

synchronous generator, making it a natural fit for both static and transient power regulation alongside ac and dc subgrids. The proposed unified modeling method also enables quantitative analysis of the system responses.

The contributions of this article are summarized as follows.

- 1) A unified static and transient power regulation modeling approach is presented for hybrid ac/dc/DS MGs, transforming the ac, dc, and DS subgrids into Thevenin's dynamic equivalent circuit models, facilitating quantitative analysis of static and transient power flow regulation.
- 2) Within DS subgrid, storage systems with slow response speeds simulate the damping loop of a synchronous generator, managing low-frequency load. High-speed storage systems simulate the inertia loop to cover high-frequency load, optimizing the operation of different storage units. The overall dynamic performance of HESS can be emulated as a synchronous generator, which lays down the cornerstone of leveraging on HESS to manage overall system inertia of the hybrid MG. Note that the presented power coordination is a general approach that can be extended to other types of HESS, such as a battery-supercapacitor, a flow battery-lithium-ion battery system.
- 3) The DS subgrid is smoothly integrated into the full-time-scale regulation of ac/dc/DS MG. Leveraging the global dynamic circuit model, the droop coefficients are flexibly designed to manage static power interactions across ac, dc, and DS subgrids. Additionally, HESS's integral droop (ID) loop maximizes its potential for global inertial regulation, improving voltage and frequency dynamic responses.

The remainder of this article is structured as follows. Section II discusses the configuration of hybrid ac/dc/DS MGs and elaborates on flexible inertia regulation. Section III presents equivalent circuit models that reveal the mechanism of tri-lateral inertia transfer among different subgrids. Sections IV and V validate the proposed unified static and transient power regulation model through simulations and experiments. Finally, Section V concludes the article.

## II. HESS ENABLED HYBRID AC/DC/DS MG CONFIGURATION AND RELEVANT CONTROL STRATEGIES

### A. Hybrid AC/DC/DS MG Configuration

A detailed configuration of a hybrid ac/dc/DS MG is shown in Fig. 2, highlighting the critical subgrid buses and interlinking converters (ILCs). The system integrates two-stage ILCs—comprising dc/dc and dc/ac converters, labeled as  $ILC_1$  and  $ILC_2$ , respectively—between the dc and ac subgrid buses. The architecture that ESSs are integrated directly bus without converters has a poor control freedom, which means the power of ESSs cannot be managed effectively. To give full play to the static and transient power regulation capabilities of ESS, a HESS is integrated into the dc-link of the two-stage ILC through converters to regulate power flow between subgrids. This architecture ensures that DERs and loads are connected directly to their respective subgrid buses, minimizing unnecessary power conversion stages, and reducing the energy transformation losses.

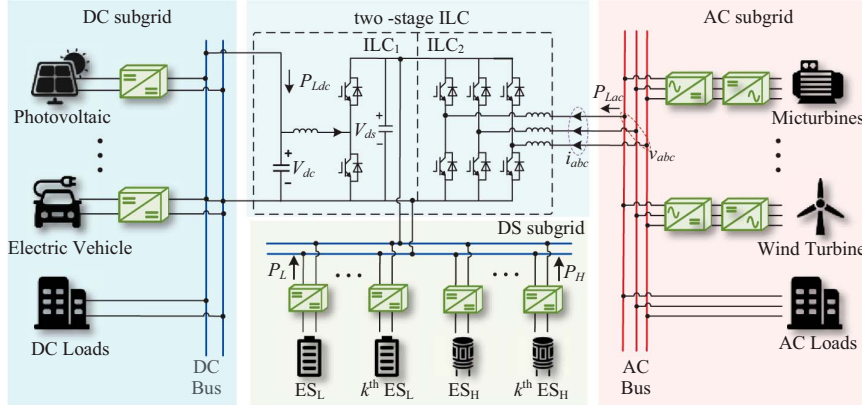


**Fig. 2.** System configuration of a hybrid ac/dc/DS MG.

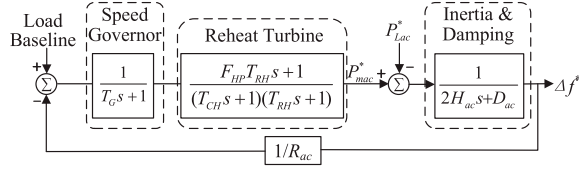


**Fig. 3.** Control diagram of frequency regulation in typical power system.

The two-stage ILC, operating in power control mode, manages efficiently power transfer across the subgrids.

### B. Virtual Inertia Control Scheme

In typical power systems, synchronous generators provide inertia to help regulate frequency changes during load fluctuations. The control framework of frequency regulation in a synchronous generator, depicted in per-unit (p.u.) terms, is shown in Fig. 3. In this figure,  $T_G$  represents the time constant of the speed governor, and the reheat turbine is characterized by three coefficients:  $F_{HP}$ ,  $T_{CH}$ , and  $T_{RH}$ . Parameter  $R_{ac}$  denotes the equivalent droop coefficient of ac system [14]. The well-known swing equation, representing system inertia and damping, is captured through the inertia and damping blocks. To facilitate a unified investigation of frequency regulation performance across synchronous generators and converters with varying rated powers, all relevant parameters are expressed in p.u. values [18]. Specifically, the mechanical power  $P_{mac}^*$  and the output power  $P_{Lac}^*$  are normalized by dividing it by their respective rated power, while the frequency deviation  $\Delta f$  is divided by its maximum value  $f_{max}$  to obtain the p.u. value  $\Delta f^*$ . For clarity, the prefix “ $\Delta$ ,” subscript “ref,” and subscript “\*” indicate changes, references, and p.u. values. This approach ensures consistency and comparability when analyzing frequency regulation across different power devices.

As outlined in [12], inertia-based control can be applied not only to ac systems but also extended to dc systems to enhance the system inertia. The control block for ac systems, including inertia and damping control, is shown in Fig. 3

$$P_{mac}^* - P_{Lac}^* = 2H_{ac} \frac{d\Delta f^*}{dt} + D_{ac} \Delta f^* \quad (1)$$

where  $H_{ac}$  represents the inertia coefficient, while  $D_{ac}$  signifies the damping coefficient in ac system.

When the system reaches a steady state, the mechanical power  $P_{mac}^*$  and output power  $P_{Lac}^*$  will reach their references  $P_{mac\_ref}^*$  and  $P_{Lac\_ref}^*$ , respectively. When small signal modeling in frequency is of interest, it is possible to subtract these steady-state reference values from (1), which can be expressed by

$$\Delta P_{mac}^* - \Delta P_{Lac}^* = 2H_{ac} \frac{d\Delta f^*}{dt} + D_{ac} \Delta f^*. \quad (2)$$

Similarly, the small signal model of dc voltage dynamics share the same form of (2) [12], and it can be described as (3), where the parameters are similar to those of the ac system and they are distinguished by the subscript “dc”

$$\Delta P_{mdc}^* - \Delta P_{Ldc}^* = 2H_{dc} \frac{d\Delta V_{dc}^*}{dt} + D_{dc} \Delta V_{dc}^* \quad (3)$$

where  $\Delta V_{dc}^*$  indicates p.u. dc bus voltage deviation.

### C. Control of AC, DC, and DS Subgrids

The integration of DERs into hybrid ac/dc/DS MGs via low-inertia interface converters leads to a substantial reduction in system inertia. Therefore, it is desirable to reshape the control loop of power converters to mimic the dynamic characteristics of synchronous generators. Fig. 4 shows how the synchronous generator features can be integrated into the conventional droop controls in p.u. domain. To better visualize the control diagram, the transfer functions of the speed governor and reheat turbine are represented by  $T(s)$  and  $Y(s)$ , respectively.  $g_{dc}$ ,  $g_{ac}$  represent the gate signals for converters of dc and ac subgrids.  $R_{dc}$  and  $R_{ac}$  are equivalent droop coefficients of dc and ac subgrids, respectively.  $V - P$  droop in dc MG and  $f - P$  droop in ac MG have been explored and documented in the existing literature [12], [13], [14], [15], and they will not be elaborated in this article. It is worth noting that the dynamic response of virtual inertia loop is far slower than the inner dual-loop control loop. Thereby, the dynamic response of subgrids is dominated by virtual inertia loop, while the inner loop gain is viewed as unity.

In the DS subgrid composed of HESS, energy storages (ESs) can be classified into a cluster of low ramp rate ESs ( $ES_L$ ) and a cluster of high ramp rate ESs ( $ES_H$ ).  $ES_L$  is expected to handle relatively slowly varying load demand components. In this

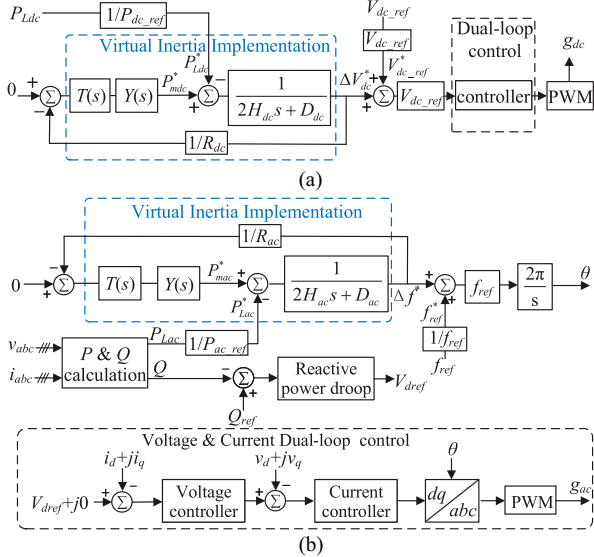


Fig. 4. Control block diagrams of ac and dc subgrids. (a) DC subgrid. (b) AC subgrid.

article, traditional  $V-P$  droop control is implemented in  $ES_L$ , as described by (4), which assumes that the line impedance between HESS's converter and DS bus is almost zero. This is reasonable for  $ES_L$  and  $ES_H$  are centrally integrated close to the DS bus. Therefore, the p.u. output voltages of  $ES_L$  and  $ES_H$  is equal to p.u. DS bus voltage  $v_{ds}^*$ , ignoring the line impedance

$$V_{ds}^* = V_{ds\_ref}^* - \frac{1}{y_L} P_L^* \quad (4)$$

where  $P_L^*$  denotes the p.u. output power of  $ES_L$ , which is equal to the ratio of the output power  $P_L$  to its reference power  $P_{ds\_ref}$ . And  $P_{ds\_ref}$  is equal to the maximum capacity of the DS subgrid.  $1/y_L$  is the droop coefficient of  $ES_L$ . It should be noted the droop control shown in (4) could help to achieve autonomous power sharing. When the HESS includes multiple  $ES_L$ , the output power of each  $ES_L$  would be proportional to their respective maximum capacity.

Compared to  $ES_L$ ,  $ES_H$  exhibits faster response speed. This characteristic gives  $ES_H$  an inherent advantage in handling the high-frequency portion of the load power. The control of  $ES_H$  can be designed by replacing the traditional droop control with integral droop (ID), as described by (5) [19]

$$V_{ds}^* = V_{ds\_ref}^* - \frac{1}{y_H} \int P_H^* dt \quad (5)$$

where  $P_H^*$  denotes p.u. output power of  $ES_H$ .  $1/y_H$  is ID coefficient.

It is worth noting that, in the DS subgrid,  $ES_L$  and  $ES_H$  should be coordinately operated. The total power demand of the DS subgrid  $P_{Lds}$  is jointly fulfilled by  $ES_L$  and  $ES_H$

$$P_L + P_H = P_{Lds} \quad (6)$$

Because the output power references of  $P_L$ ,  $P_H$ , and  $P_{Lds}$  are all equal to the maximum capacity of the DS subgrid, (6) in p.u. domain can be expressed by

$$P_L^* + P_H^* = P_{Lds}^* \quad (7)$$

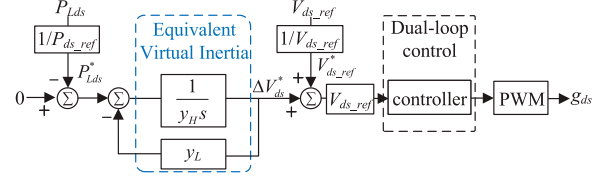


Fig. 5. Equivalent control diagram of DS subgrid.

To clarify the power allocation between  $ES_L$  and  $ES_H$ , by combining (4), (5), and (7), the Laplace domain expressions of  $P_L^*$  and  $P_H^*$  are seen as

$$P_L^* = \frac{y_L/y_H}{s + y_L/y_H} P_{Lds}^* \quad (8)$$

$$P_H^* = \frac{s}{s + y_L/y_H} P_{Lds}^* \quad (9)$$

where  $s$  is the Laplace operator. According to (4)–(9), the HESS is uniformly controlled under voltage source mode without switching the operating modes.

In fact,  $ES_L$  does not have to be lead carbon battery, and  $ES_H$  also does not have to be super-capacitor, as this article does. For example, when it comes to the situation that a flow battery and a lithium-ion battery are combined to form a hybrid energy storage system, the flow battery has comparatively low ramp rate while the lithium-ion battery has comparatively high ramp rate. Then, similar to this article,  $V-P$  droop control can be implemented for flow battery and ID can be implemented for the lithium-ion battery. By means of this control set up, transient power coordination can also be achieved.

It is seen from (8) and (9) that the power demand is autonomously decomposed into high/low-frequency components and allocated to  $ES_L$  and  $ES_H$ , respectively. Transient power allocation between  $ES_L$  and  $ES_H$  can be regulated by changing the ratio of droop coefficients  $y_L/y_H$ . Rearranging (6)–(9), in per unit domain, the holistic dynamic correlation between the output power change  $\Delta P_{Lds}^*$  given by the DS subgrid and DS bus voltage deviation  $\Delta V_{ds}^*$  can be derived by

$$\frac{\Delta V_{ds}^*}{\Delta P_{Lds}^*} = \frac{1}{y_H s + y_L}. \quad (10)$$

With the help of (10), it is possible to obtain the equivalent control block diagram of the DS subgrid shown in Fig. 5. Comparing the control diagrams in Figs. 3 and 5, it is found that, the consolidation of ID and traditional  $V-P$  droops naturally formulate the control diagram which shares the same format as the swing equation of a synchronous generator, disregarding the speed governor and reheat turbine transfer functions. Although virtual inertia and damping are not intentionally integrated into the control loops, ID can resemble the characteristics of virtual inertia and the conventional droop brings in damping effects to the DS subgrid. This fact facilitates the integration of DS subgrid control dynamics into the entire hybrid system controls. On one hand, dynamic power sharing between  $ES_L$  and  $ES_H$  can be autonomously realized. On the other hand, modifying the integral and conventional droop coefficients helps to flexibly adjust

inertia response and global power sharing. More detailed explanations will be given in Section III and onward.

It is worth pointing out that the derivation of (4)–(10) assumes that the HESS is centrally integrated close to the DS bus. If  $ES_L$  and  $ES_H$  are dispersed across the ac and dc subgrids, it unavoidably results in different line impedances between the HESS and the bus, owing to the deployment of various ESSs to distinct geographical locations. Consequently, the high- and low-frequency power decomposition of  $ES_L$  and  $ES_H$  becomes inaccurate without line impedance compensation in the control strategy.

If a  $ES_L$  and a  $ES_H$  are linked to a common bus via impedances, the droop should be revised accordingly as follows:

$$\begin{cases} V_{ds} = V_{ds\_ref} - \frac{1}{y_L} P_L - i_L R_L \\ V_{ds} = V_{ds\_ref} - \frac{1}{y_H s} P_H - i_H R_H \end{cases} \quad (11)$$

where  $R_L$  and  $i_L$  denote the impedance and output current of  $ES_L$  converter, respectively.  $R_H$  and  $i_H$  denote the impedance and output current of  $ES_H$  converter, respectively. Note that  $P_L = i_L V_{ds}$  and  $P_H = i_H V_{ds}$ . The load current equals the total output of  $ES_L$  and  $ES_H$  converters, and its small signal expression can be shown below

$$\Delta i_L + \Delta i_H = \Delta i_{Lds}. \quad (12)$$

Combining (11) and (12), the output current of the  $ES_L$  and  $ES_H$  in the Laplace domain is given as follows:

$$\begin{cases} \Delta i_L = \frac{y_L y_H R_H / V_{ds} s + y_L}{[y_H(1 + y_L R_L) + y_L y_H R_H] s / V_{ds} + y_L} \Delta i_{Lds} \\ \Delta i_H = \frac{y_H(1 + y_L R_L / V_{ds}) s}{[y_H(1 + y_L R_L) + y_L y_H R_H] s / V_{ds} + y_L} \Delta i_{Lds}. \end{cases} \quad (13)$$

To better illustrate the inaccurate decomposition of high/low frequency power caused by line impedance, Fig. 6 compares the Bode diagrams of  $i_L$  and  $i_H$  with negligible and non-negligible line impedance ( $R_L = 2\Omega$  and  $R_H = 1\Omega$ ). It can be observed that  $i_L$  with line impedance is around  $-10.1$  dB in the high-frequency range, while  $i_L$  without line impedance is much lower. Conversely,  $i_H$  is significantly smaller when line impedance is present. This indicates that in the presence of line impedance, a portion of the high-frequency current from  $ES_H$  “leaks” into  $ES_L$ , subjecting the battery to rapid current fluctuations that may reduce its lifespan. In contrast, the centralized deployment of HESS close to bus brings comparable line impedance between  $ES_L$  and  $ES_H$ , enabling uniform compensation strategies to counteract impedance effects [20]. However, if ESSs are dispersed in dc and ac subgrids, obtaining line impedance is laborious since each ESS is deployed at a different location. In addition, this necessitates specific compensation protocols for individual ESS converter, escalating ESS control complexity.

#### D. Control of Two-Stage ILC

In prior discussion, it has demonstrated how ac, dc, and DS subgrids behave under various inertia control mechanisms in transient process and steady state. For the hybrid ac/dc/DS MG under study, as shown in Fig. 2, the three subgrids are coupled

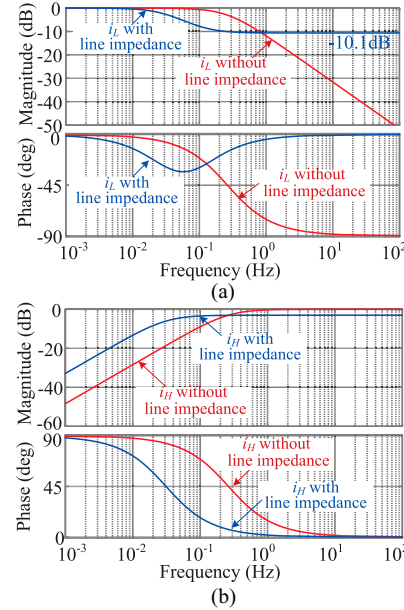


Fig. 6. Bode diagrams of  $i_L$  and  $i_H$  with and without line impedances. (a) Bode diagrams of  $i_L$ . (b) Bode diagrams of  $i_H$ .

via the two-stage ILC. Before the ILC is activated, each subgrid is operated separately. In the case of the ILC being enabled, tri-lateral power exchange in three subgrids would take place, which allows for the regulations of transient and static power flows. For dc subgrid, the bus voltage drop caused by sudden load step-up encapsulates the inertia information, whereas the bus voltage deviation from the reference value in steady state reveals loading condition of the dc system [21]. Obviously, in the situation of high inertia, dc bus voltage drop/surge would be lesser during transient load-change process. At the end of the system transition, the dc system with less capacity exhibits larger voltage deviation. Similar reasoning also applies to ac and DS subgrids. It should be mentioned that, for both transient and static responses in the hybrid system, the quantities (i.e., voltage or frequency) expressed in SI units are incomparable, which causes difficulties to generate a proper control law to the ILC. To address this problem, per unit values of the critical electrical quantities are employed. For instance, the power reference  $P_{ref1}$  of ILC<sub>1</sub> is calculated based on the difference between the p.u. values of dc and DS subgrid bus voltages, which is given by

$$P_{ref1}^* = (V_{ds}^* - V_{dc}^*) \left( k_{p1} + \frac{k_{i1}}{s} \right) \quad (14)$$

where  $k_{p1}$  and  $k_{i1}$  represent the proportional and integral coefficients of the PI controller in ILC<sub>1</sub>. A corresponding control diagram of ILC<sub>1</sub> can be visualized in Fig. 7(a).

The power reference  $P_{ref2}$  of ILC<sub>2</sub> can be designed in the same way by replacing the term  $V_{dc}^*$  in (14) with p.u. ac frequency  $f^*$ , the reference value of power transfer in ILC<sub>2</sub> can be written as

$$P_{ref2}^* = (V_{ds}^* - f^*) \left( k_{p2} + \frac{k_{i2}}{s} \right) \quad (15)$$

where  $k_{p2}$  and  $k_{i2}$  represent the proportional and integral coefficients of the PI controller in ILC<sub>2</sub>. A corresponding control diagram of ILC<sub>2</sub> can be visualized in Fig. 7(b).

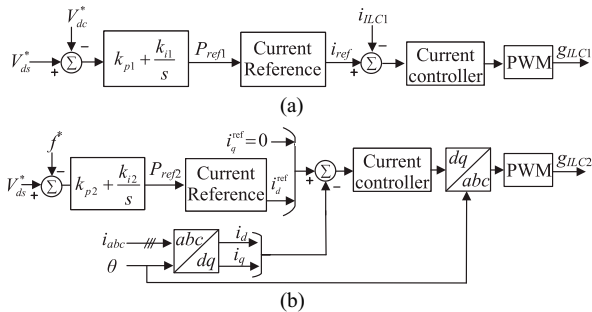


**Fig. 7.** Control diagram of the two-stage ILC. (a) ILC<sub>1</sub>. (b) ILC<sub>2</sub>. (Configuration of ILC<sub>1</sub> and ILC<sub>2</sub> shown in Fig. 2.)

According to (14), the reference value for the power delivered by ILC<sub>1</sub> is the transfer function of PI controller multiplied by the error between the normalized dc and DS bus voltages. Since the control bandwidth of PI control is designed to be high, the error will quickly go to zero. When the dc subgrid faces load fluctuations, ILC<sub>1</sub> actively transfers the load of the dc subgrid to the DS subgrid to keep the p.u. dc and DS bus voltages consistent. The same regulation process occurs between DS and ac subgrids due to the control of ILC<sub>2</sub>.

### III. UNIFIED STATIC AND TRANSIENT POWER REGULATION MODEL FOR HYBRID AC/DC/DS MGs

#### A. Unified Static and Transient Power Modeling

Section II exhibits the control methods of various components within ac/dc/DS MG. By observing Figs. 4 and 5, it can be found that comparable virtual inertia blocks are present within the control diagrams. The comparability of controls facilitates the modeling of different subgrids in a unified form. By incorporating the power control of ILC, each subgrid model are smoothly integrated, thereby establishing a unified static and transient power regulation modeling.

Power change in an ac system influences the frequency, whereas in a dc or DS system, it impacts the bus voltage. The different physical units of voltage and frequency pose a challenge for the analysis of unified power regulation. This article proposes a unified power regulation model established in p.u. domain, eliminating the influence of different physical units. According to the control block diagrams in Figs. 4 and 5, the transfer functions from the load changes to the bus voltage/frequency fluctuations in p.u. domain can be expressed by

$$\begin{cases} \frac{\Delta V_{dc}^*}{\Delta P_{Ldc}^*} = \frac{-R_{dc}}{(2H_{dc}s + D_{dc})R_{dc} + T(s)Y(s)} = -Z_{dc} \\ \frac{\Delta V_{ac}^*}{\Delta P_{Lac}^*} = \frac{-R_{ac}}{(2H_{ac}s + D_{ac})R_{ac} + T(s)Y(s)} = -Z_{ac} \\ \frac{\Delta V_{ds}^*}{\Delta P_{Lds}^*} = \frac{-1}{y_{HS} + y_L} = -Z_{ds}. \end{cases} \quad (16)$$

For simplicity,  $U = \text{col}(\Delta V_{dc}^*, \Delta f^*, \Delta V_{ds}^*)$  represents the column vector of p.u. bus voltage/frequency deviation.  $I_p = \text{col}(\Delta P_{Ldc}^*, \Delta P_{Lac}^*, \Delta P_{Lds}^*)$  represents the column vector of p.u. subgrid power change.

Since the droop control with virtual inertia implementation is applied in each subgrid, there are dynamic deviations in bus

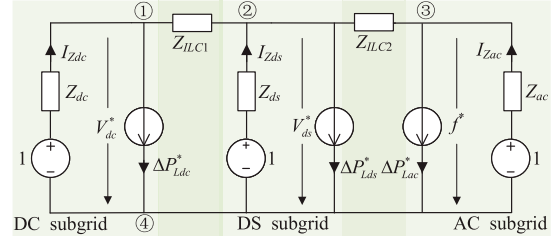


**Fig. 8.** Global equivalent circuit model of the hybrid ac/dc/DS MG.

voltage or frequency from their respective reference values. The bus voltage or frequency in the entire time domain can be derived by

$$W = M - ZI_p \quad (17)$$

where  $W = \text{col}(V_{dc}^*, f^*, V_{ds}^*)$ ,  $M = \text{col}(1, 1, 1)$  denotes the unit column vector.  $Z = \text{diag}(Z_{dc}, Z_{ac}, Z_{ds})$  represents impedance matrix of global ECM.

In the hybrid ac/dc/DS MG, the global load is distributed to the ac, dc, and DS subgrids through the two-stage ILC. The properties of the ILC should be modeled to drive the establishment of the unified power regulation model. According to (14) and (15), the relationship between the deviations of variables  $V_{dc}^*$ ,  $f^*$ ,  $V_{ds}^*$ , and the power scheduled by the ILC can be expressed as follows:

$$Z_{ILCn} = \frac{s}{k_{pn}s + k_{in}} \quad (18)$$

where  $n$  represents the index of the ILC, which can take a value of 1 or 2.  $k_{pn}$  and  $k_{in}$  represent the proportional and integral coefficients of the PI controllers in the ILC<sub>1</sub> and ILC<sub>2</sub>.

In (17), the voltage and frequency are expressed in per unit form, indicating that they are devoid of physical units. Assuming that  $W$  refers to the unit voltage source and  $I_p$  refers to the current source, (17) resemble the format of Thevenin equivalent circuit, where  $Z$  inherently represent impedance. Therefore, the dynamic characteristics of dc, DS bus and ac frequency can be visualized by Thevenin circuits. Furthermore, with the help of (18), the ports of each Thevenin equivalent circuit can be interconnected by  $Z_{ILCn}$ . Based on above steps, the unified power regulation model named the global equivalent circuit model (ECM) is established and shown in Fig. 8. Crucially, the proposed ECM provides a paradigm to quantify the response process of hybrid ac/dc/DS MG. The analysis of global ECM can be done with the help of node analysis method, as shown in the following equation:

$$GV_{node} = I_p - I_p \quad (19)$$

where  $G$  represents the node admittance matrix.  $I_p = \text{col}(1/Z_{dc}, 1/Z_{ac}, 1/Z_{ds})$  representing vector of which each element is the current injecting into the node from voltage sources.  $V_{node} = \text{col}(V_{dc}^*, f^*, V_{ds}^*)$  denotes node voltage vector of which each element is the node voltage in Fig. 8.

Although the static and transient power of each subgrid can be quantitatively calculated by the global ECM, the existence of  $Z_{ILCn}$  increases the computational complexity. The global ECM will be further simplified by exploring the full frequency

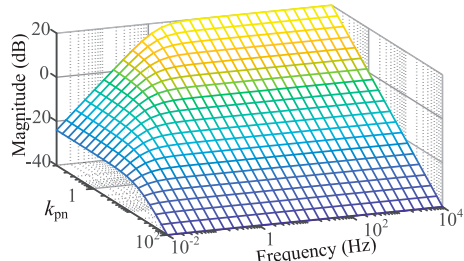


**Fig. 9.** Amplitude–frequency response of  $Z_{ILCn}$  when  $k_{pn}$  varies and  $k_{in}$  is fixed at 1.

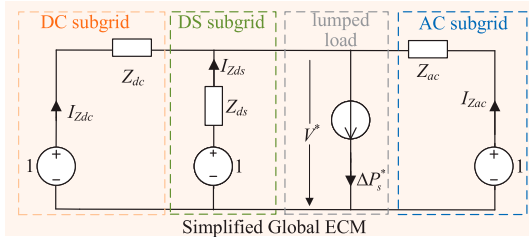


**Fig. 10.** Simplified global equivalent circuit model of the hybrid ac/dc/DS MG in Fig. 8.

response of  $Z_{ILCn}$  to obtain a more concise and intuitive global ECM. The amplitude-frequency response of  $Z_{ILCn}$  changes with  $k_{pn}$  as shown in Fig. 9. Regardless of the value of  $k_{pn}$ , the amplitude-frequency response of  $Z_{ILCn}$  remains significantly less than 0 dB in the low frequency band. As  $k_{pn}$  increases, the amplitude-frequency response of  $Z_{ILCn}$  gradually decreases in the high frequency band. To achieve transient power control,  $k_{pn}$  is usually large enough to improve the response speed of ILC. Therefore, the amplitude-frequency response of  $Z_{ILCn}$  is significantly below 0 dB in all frequency bands.  $Z_{ILCn}$  can be regarded as a negligible impedance. In this case, the simplified global ECM is shown in Fig. 10, where the global current source  $\Delta P_s^*$  can be derived by

$$\Delta P_s^* = \Delta P_{Ldc}^* + \Delta P_{Lac}^* + \Delta P_{Lds}^*. \quad (20)$$

According to the simplified global ECM shown in Fig. 10, it can be found that the impedance current is inversely proportional to the subgrid impedance, as shown by

$$I_{Zdc} : I_{Zac} : I_{Zds} = \frac{1}{Z_{dc}} : \frac{1}{Z_{ac}} : \frac{1}{Z_{ds}} \quad (21)$$

where  $I_{Zdc}$ ,  $I_{Zac}$  and  $I_{Zds}$  denotes the current flowing through subgrid impedance, respectively.

In the simplified ECM, the p.u. output power of subgrids is quantified by the current traversing respective impedances. Analytical derivation in (21) reveals that subgrid impedance constitutes the principal determinant of output power dynamics. To elucidate the static and transient power regulation characteristics across dc, ac, and DS subgrids, the frequency-domain behavior of impedances  $Z$  is illustrated in Bode diagrams of Fig. 11, while critical hybrid ac/dc/DS MG parameters are listed in Table III.

On one hand, the low-frequency region of the Bode diagrams corresponds to static power allocation. It is observed that the

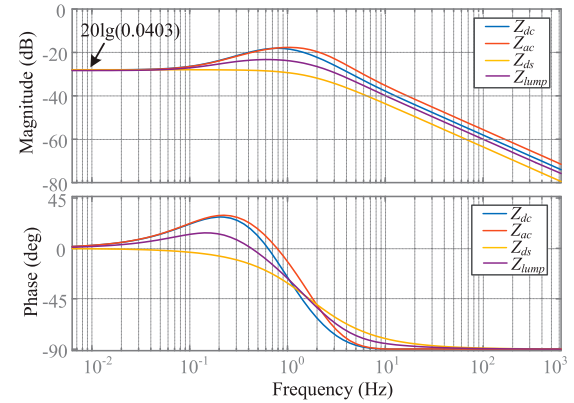


**Fig. 11.** Bode diagrams of  $Z_{dc}$ ,  $Z_{ac}$ ,  $Z_{ds}$  and  $Z_{lump}$  when  $H_{dc} = 3$  s,  $H_{ac} = 4$  s and  $H_{ds} = 7.5$  s.

low-frequency impedances of the three subgrids converge to the same magnitude [ $-27.959$  dB =  $20 \lg(0.04)$ ], indicating that  $I_{Zdc}$ ,  $I_{Zac}$ , and  $I_{Zds}$  (i.e.,  $P_{Ldc}/P_{Ldc\_ref}$ ,  $P_{Lac}/P_{Lac\_ref}$ , and  $P_{Lds}/P_{Lds\_ref}$ ) are equal under steady-state conditions. Consequently, each subgrid delivers power proportionally to its maximum capacity during steady-state operation. On the other hand, the high-frequency region of the Bode diagrams reflects transient power allocation. Based on (16) and (21), the transient power contribution of each subgrid is positively correlated with its inertia. Therefore, increasing the inertia of the DS subgrid enables it to absorb a larger share of transient power, thereby alleviating the transient power burden on the dc and ac subgrids. The parameter design for system static and transient regulation is further elaborated in Section III-B.

### B. Full Time-Scale Regulations Through DS Subgrid

In the unified static and transient power model, the output power of each subgrid depends on the dynamic impedance. According to (16), changing the traditional  $V$ - $P$  droop coefficient  $y_L$  and ID coefficient  $y_H$  is equivalent to changing the impedance of the DS subgrid. This observation serves to explore the full-time scale regulation based on designing the traditional and ID coefficient of HESS. In static state, the static power sharing can be calculated by setting the Laplace operator ‘ $s$ ’ in (16) to zero

$$\begin{cases} Z_{dc\_low} = \frac{R_{dc}}{D_{dc}R_{dc} + 1} \\ Z_{ac\_low} = \frac{R_{ac}}{D_{ac}R_{ac} + 1} \\ Z_{ds\_low} = \frac{1}{y_L} \end{cases} \quad (22)$$

where  $Z_{dc\_low}$ ,  $Z_{ac\_low}$ , and  $Z_{ds\_low}$  refer to the low-frequency impedance of each subgrid. The static global power sharing among ac, dc, and DS subgrids, can be obtained as in the following equation:

$$\begin{aligned} I_{Zdc} : I_{Zac} : I_{Zds} &= \frac{1}{Z_{dc\_low}} : \frac{1}{Z_{ac\_low}} : \frac{1}{Z_{ds\_low}} \\ &= \frac{D_{dc}R_{dc} + 1}{R_{dc}} : \frac{D_{ac}R_{ac} + 1}{R_{ac}} : y_L. \end{aligned} \quad (23)$$

In transient state, the performance of bus voltage or frequency is an important topic, as rapid drops in voltage or frequency may cause rate-of-change protection devices to falsely activate and result in system load shedding. Benefiting from the proposed global ECM illustrated in Fig. 8, the p.u. dc voltage, DS bus voltage, and ac frequency are equivalently represented as the terminal voltages on global current source (GCS), as shown by

$$f^* = V_{dc}^* = V_{ds}^* = V^* \quad (24)$$

where  $V^*$  means the terminal voltage across global current source. It should be noted that, for all ac, dc, and DS subgrids, the inertia quantities, i.e.,  $H_{ac}$ ,  $H_{dc}$ , and  $y_H$  are incorporated in the corresponding impedances. When it comes to the global hybrid ac/dc/DS system, it can be inferred that the total inertia could also be revealed by investigating the lump impedance in global EMC. The lumped impedance can be derived by

$$\begin{aligned} Z_{lump} &= Z_{dc} \parallel Z_{ac} \parallel Z_{ds} \\ &= \frac{R_1 K(s)}{(2H_G s + D_G) R_1 K(s) + R_2 (s F_{HP} T_{RH} + 1)} \end{aligned} \quad (25)$$

$$\begin{aligned} H_G &= \left( \frac{y_H}{2} + H_{ac} + H_{dc} \right), D_G = (D_{ac} + D_{dc} + y_L), R_1 = R_{dc} R_{ac} \\ R_2 &= R_{dc} + R_{ac}, K(s) = (1 + s T_{RH}) (1 + s T_G) (1 + s T_{CH}) \end{aligned}$$

where  $H_G$  and  $D_G$  can be regarded as the global inertia and damping, respectively.

Owing to the fact that two corresponding zero and pole points in (25) will cancel each other as the inertia increases [22], (25) can be simplified into the following equation:

$$\begin{aligned} Z_{lump} &= \frac{R_1 (1 + s T_{RH})}{(2H_G s + D_G) (1 + s T_{RH}) R_1 + R_2 (s F_{HP} T_{RH} + 1)} \\ &= G_0 \frac{s + z_1}{s^2 + 2\zeta\omega_n s + \omega_n^2} \end{aligned} \quad (26)$$

where

$$\begin{aligned} G_0 &= \frac{1}{2H_G}, \quad z_1 = \frac{1}{T_{RH}}, \quad \omega_n = \sqrt{\frac{D_G R_1 + R_2}{2H_G R_1 T_{RH}}} \\ \zeta &= \frac{H_G R_1 + D_G R_1 T_{RH} + R_2 F_{HP} T_{RH}}{2H_G R_1 T_{RH}} \cdot \sqrt{\frac{2H_G R_1 T_{RH}}{D_G R_1 + R_2}} \end{aligned}$$

$\omega_n$  and  $\zeta$  represent the undamped natural frequency and damping ratio, respectively.

Assuming that a step-up load change occurs,  $V^*$  can be expressed in the Laplace domain as follows:

$$\begin{aligned} V^*(s) &= \underbrace{V_{ref}^*(s)}_{\text{Reference}} - \underbrace{\frac{Z_{lump}}{s}}_{\text{Deviation}} \\ &= \frac{1}{s} - G_0 \left\{ \left[ \frac{1}{s} + \frac{1}{\left( \frac{T_2}{T_1} - 1 \right) \left( s + \frac{1}{T_1} \right)} + \frac{1}{\left( \frac{T_1}{T_2} - 1 \right) \left( s + \frac{1}{T_2} \right)} \right] \right\} \\ &\quad \left\{ \frac{1}{s} \cdot \frac{s}{s^2 + 2\zeta\omega_n s + \omega_n^2} + \frac{z_1}{\omega_n^2} \right\} \end{aligned} \quad (27)$$

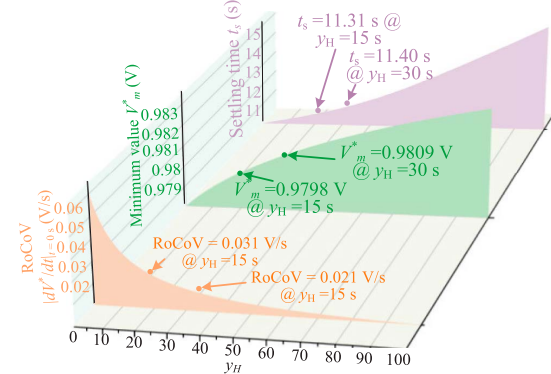


Fig. 12. RoCoV and settling time  $t_s$  versus different  $y_H$ .

TABLE I  
KEY TRANSIENT PARAMETERS CALCULATED IN SI DOMAIN

Integral Droop Coefficient ( $1/y_H$ )	RoCoV or RoCoF	The Minimum Values	Settling Time $t_s$
1/15	RoCoV = 11.78 V/s RoCoF = 1.58 Hz/s	372.32 V 49.97 Hz	11.31 s
1/30	RoCoV = 7.98 V/s RoCoF = 1.07 Hz/s	372.74 V 50.03 Hz	11.5 s

where  $T_1$  and  $T_2$  are time constants, which can be calculated by

$$T_1 = \frac{1}{\omega_n(\xi - \sqrt{\xi^2 - 1})}, \quad T_2 = \frac{1}{\omega_n(\xi + \sqrt{\xi^2 - 1})}. \quad (28)$$

Performing the inverse Laplace transformation of (27), the time domain expression of  $V^*$  can be shown as

$$V^*(t) = 1 - G_0 \left[ \frac{\frac{T_1 T_2 (e^{-t/T_2} - e^{-t/T_1})}{T_2 - T_1} + \frac{z_1}{\omega_n^2} \left( 1 + \frac{T_2}{T_2 - T_1} e^{-t/T_1} + \frac{T_1}{T_1 - T_2} e^{-t/T_2} \right)}{z_1 \left( 1 + \frac{T_2}{T_2 - T_1} e^{-t/T_1} + \frac{T_1}{T_1 - T_2} e^{-t/T_2} \right)} \right]. \quad (29)$$

The derivative of (29) is used to evaluate the rate of change of voltage (RoCoV) of GCS, which is expressed by (30). In general, the RoCoV of global current source is greatest at the beginning of load disturbance ( $t = 0$ )

$$\frac{dV^*(t)}{dt} = -G_0 \left( \frac{z_1 e^{-t/T_1} - e^{-t/T_2}}{\omega_n^2} + \frac{T_2 e^{-t/T_1} - T_1 e^{-t/T_2}}{T_1 - T_2} \right). \quad (30)$$

The nadir time  $t_{nadir}$  denotes the moment when  $V^*$  reaches its minimum value, which can be derived by setting (30) to zero

$$\frac{dV^*(t)}{dt} = 0. \quad (31)$$

The voltage minimum  $V_m^*$  can be calculated by substituting the nadir time into (29)

$$V_m^* = V^*(t_{nadir}). \quad (32)$$

The steady state voltage can be obtained by setting  $t$  in (29) to infinity, which can be represented as

$$V_{\text{steady}}^* = 1 - \frac{G_0 z_1}{\omega_n^2} = 1 - \frac{R_1}{D_G R_1 + R_2}. \quad (33)$$

**TABLE II**  
COMPARISONS BETWEEN DYNAMIC CIRCUIT-BASED UNIFIED POWER REGULATION AND EXISTING METHODS

References	Improving AC MG Dynamic Characteristics	Improving DC MG Dynamic Characteristics	System With Multilateral Inertia Source	Quantify the Inertia for Microgrids Given Specific Requirements	Calculation of Dynamic Indicators
[24], [25], [26]	✓	✗	✓	✗	✗
[9], [27], [28]	✓	✓	✓	✗	✗
[13]	✓	✓	✓	✗	✗
[12]	✓	✓	✓	✗	✗
[22]	✗	✓	✗	✗	✓
This article	✓	✓	✓	✓	✓

The settling time  $t_s$  (time for entering the 5% steady-state error band) commonly denotes the duration required for a system to attain stable state, which can be derived by

$$\left| \frac{V^*(t_s) - V_{\text{steady}}^*}{V_{\text{steady}}^* - 1} \right| = 5\% \quad (34)$$

$$[V_{\text{dc}}, f, V_{\text{dc}}] = V_m^* [V_{\text{dc\_max}}, f_{\text{max}}, V_{\text{ds\_max}}]. \quad (35)$$

Based on (26) to (34), Fig. 12 visualizes the key transient indicators (RoCoV, the minimum value  $V_m^*$ , and settling time  $t_s$ ) versus different  $y_H$  under a 30% load step. The critical parameters of hybrid ac/dc/DS MG are listed in Table III. Notably,  $V^*$  is defined in p.u. domain, whereby transient performance metrics must be scaled by their corresponding reference values to derive actual values as shown in (35). Table I lists actual values of transient indicators with  $y_H$  set as 15 and 30. The RoCoV/RoCoF and maximum transient deviation  $V_m^*$  are important indicators for judging the safe operation of the system. RoCoF-based relays are widely used in the UK to detect and react to loss of mains situations. To align with the stability requirements of high power-electronics-penetrated microgrids, the allowable maximum RoCoF is designed as 1Hz/s during load step transients [23]. Additionally, IEC 61727 states that the maximum transient deviation of frequency shall not exceed 1 Hz. Engineers can refer to the table converted from Fig. 12 to design the integral coefficients  $y_H$  in the DS subgrid to meet the inertia requirements. Furthermore, similar table and figure can also be obtained by performing different load changes, and they can be used as reference to engineers to design  $y_H$  in DS subgrid.

Moreover, it is easy to understand from Table I and Fig. 12 that, increasing  $y_H$  can help to increase the inertia of the entire hybrid MG, which provides a highly flexible way to tune system transient performance.

### C. Discussions

The preceding sections elaborate on the static and transient power regulation model, while the proposed methodology can be readily extended to the hybrid ac/dc/DS MG incorporating multiple DERs, ESSs, and ILCs. Taking multiple DERs with different dynamic characteristics in dc subgrid as an example, with global equivalent circuit model (see Fig. 8) in mind, each DER can be modeled as a single Thevenin equivalent circuit and connected in parallel with a current source that represents the load fluctuations.

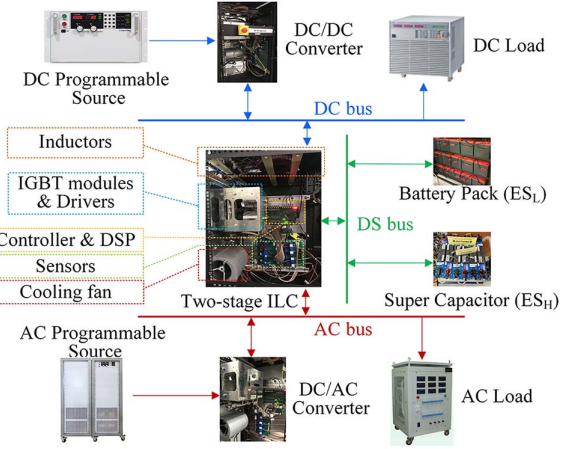


Fig. 13. Experimental platform.

By means of circuit equivalence, multiple parallel ECMs can be simplified into a consolidated ECM, where the value of the consolidated voltage source is unity and the consolidated impedance is equal to the parallel connection of the impedances in each ECM. AC subgrid and DS subgrid can also be derived in a similar way. The consolidated ECM of dc, ac, and DS subgrids are connected by the impedance representing the ILC to form a global drop of 0.04 on the ECM including multiple DERs, ESSs, and ILCs in the system. Once the global ECM is established, the static and transient power regulation of the hybrid ac/dc/DS microgrid can be derived according to the process described in Section III-A and B. In conclusion, varying numbers of DERs, ESSs, and ILCs rarely increase the complexity of modeling. This substantiates the scalability and adaptability of the model proposed unified model.

The quantification of inertia is imperatively needed in practical engineering during system planning and operating phase. However, there is almost no literature reporting how to quantify the system level inertia for hybrid ac/dc/DS MG, where ac system and dc system coexist. Moreover, rare literature reporting the insights of using hybrid energy storage system to simultaneously emulate inertia for both ac subgrid and dc subgrid. Therefore, it is safe to conclude that dynamic circuit modeling in this article is a brand-new approach to uniformly regulate static and transient power, and no similar method is found in public research. To highlights the novelty of this article, necessary comparisons between the control strategy in this article and some inertia-related papers are conducted, and the corresponding results are displayed in Table II.

**TABLE III**  
KEY SYSTEM PARAMETER SETTINGS

System Components	Parameter	Setting
DC subgrid	Input and output voltage	100 V, 380 V
	Subgrid capacity	20 kW
	Inertia and damping coefficient	$H_{dc} = 3 \text{ s}$ , $D_{dc} = 1$
AC subgrid	Input and output voltage	380 V, 710 V
	Frequency reference value	51 Hz
	Subgrid capacity	20 kW
DS subgrid	Inertia and damping coefficient	$H_{ac} = 4 \text{ s}$ , $D_{ac} = 1$
	Input and output voltage	250 V, 710 V
	Subgrid capacity	20 kW
Two-stage ILC	Traditional and integral droop coefficients	$y_H = 15$ , $y_L = 0.0403$
	DC/dc inductor $L_{ILC1}$	2 mH
Other parameters of virtual inertia	DC/ac inductor $L_{ILC2}$	2 mH
	$T_G$ , $F_{HP}$ , $T_{CH}$ , $T_{RH}$	0.1, 0.3, 0.2, 7

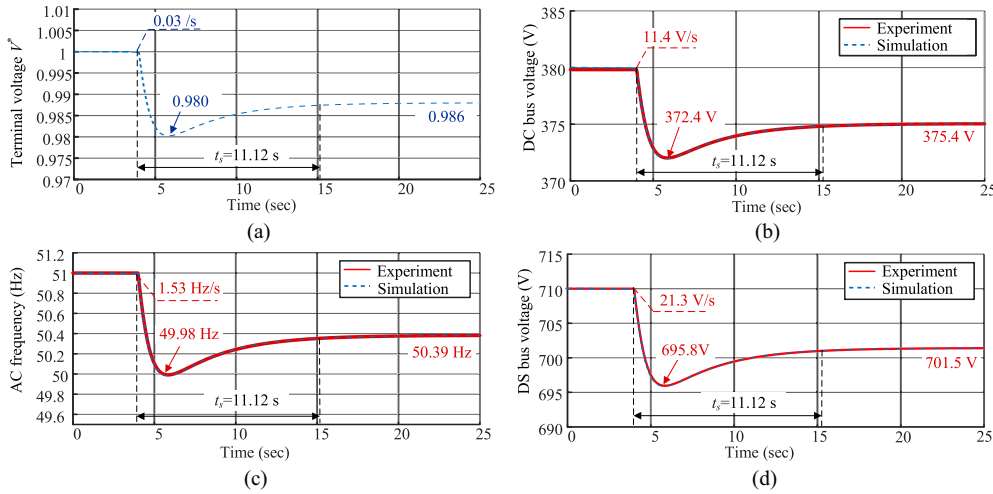


**Fig. 14.** Response process of bus voltage and frequency in a hybrid ac/dc/DS microgrid under a 30% load step ( $y_H = 15$ ). (a) Terminal voltage  $V^*$  simulation profile. (b) Comparison of dc bus voltage responses between simulation and experiment. (c) Comparison of ac frequency responses between simulation and experiment. (d) Comparison of DS bus voltage responses between simulation and experiment.

#### IV. EXPERIMENTAL VERIFICATIONS

According to the system configuration shown in Fig. 2, experiments shown in Fig. 13 were conducted in a hybrid MG to validate the effectiveness of the unified static and transient power regulation model and full time-scale regulation of HESS. Table III displays the system parameter configurations. The control algorithms were performed on a digital signal processor (DSP-TMS320F28335) together with a controller board. The dc bus was set up by a programmable dc power supply (Chroma 62100H-600S) via a droop-characterized dc/dc converter. The dc power supply (Magna-Power MTD1000-100/380) formed an ac subgrid through a dc/ac converter.  $ES_L$  and  $ES_H$  formed HESS and were connected to the dc capacitor of the two-stage ILC (a.k.a. DS bus). The power ratings of battery pack and super-capacitor pack are 14.4 and 5.6 kW.

##### A. Case 1

For validation of the correctness and accuracy of the proposed equivalent circuit model (ECM), a simplified global ECM shown in Fig. 10 is built in MATLAB/Simulink. The experimental waveforms captured via a Tektronix MDO 3

Series oscilloscope were subsequently exported to MATLAB for comparative analysis against simulation results. Fig. 14(a) shows the simulation result of  $V^*$  under a 30% load step initiated across all subgrids. Key transient metrics (RoCoV/RoCoV, the minimum value  $V_m^*$ , and settling time  $t_s$ ) are annotated in Fig. 14, which is basically consistent with the results shown in Fig. 12. Fig. 14 compare experimental measurements (solid lines) and simulation outputs (dashed lines) for dc, DS Bus Voltage and ac frequency. For quantitative comparison, the  $V^*$  is converted to the actual values according to (35). It can be observed that the simulation and experimental curves are almost the same. In addition, the transient indicators (RoCoV,  $V_m^*$  and  $t_s$ ) are very close to the results in Table I, with the maximum error not exceeding 2%. This proves the effectiveness and accuracy of the proposed dynamic equivalent circuit model. The cause of errors likely originates from measurement and model simplification.

##### B. Case 2

Fig. 15(a) shows the response of dc bus voltage and ac frequency when dc and ac grids operate independently, while

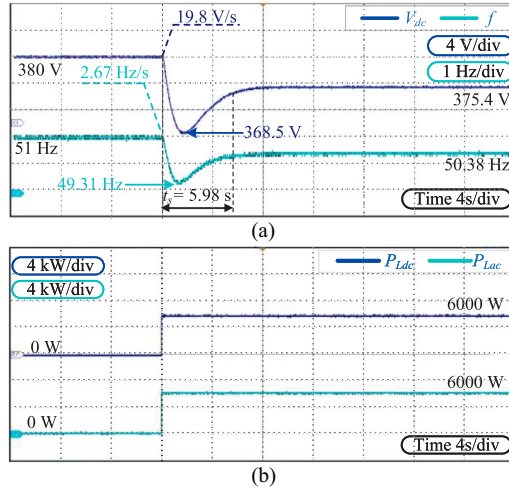


**Fig. 15.** Response process of isolated grids. (a) DC bus voltage and ac frequency response. (b) Output power of dc, ac subgrid.

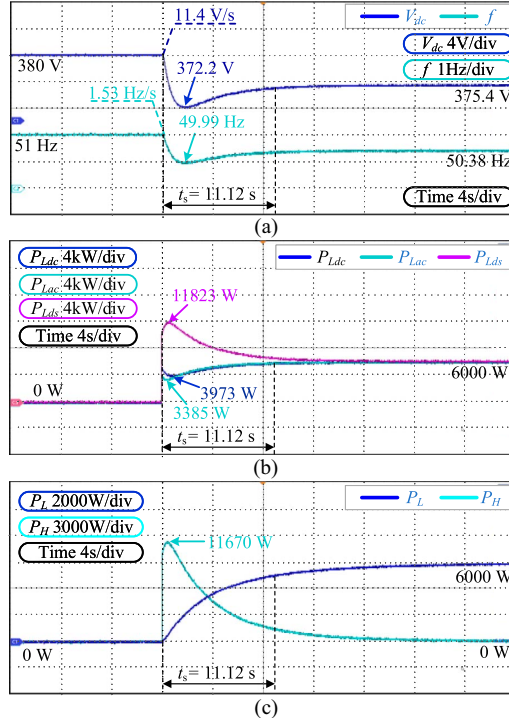


**Fig. 16.** Response process of hybrid ac/dc/DS when  $y_H = 15$ . (a) DC bus voltage and ac frequency response. (b) Output power of dc, ac, and DS subgrid. (c) Power allocation of ES<sub>L</sub> and ES<sub>H</sub> in DS subgrid.

Fig. 16(a) shows the responses of the dc bus voltage and ac frequency when the ac, dc, and DS grids form a hybrid ac/dc/DS MG. With global ECM of Fig. 10 in mind, Fig. 11 shows the Bode diagrams of impedances  $Z_{dc}$ ,  $Z_{ac}$ , and  $Z_{ds}$ . Taking the dc subgrid as an example, the low-frequency gain of its impedance can be observed at around  $-27.959$  dB. This means that a unit current will produce a voltage drop of 0.0403 on the impedance dc subgrid. This observation can be verified by the experimental results Figs. 15(a) and 16(a) where a 30% load step-up takes place. The p.u. value of load change can be denoted as 0.3, provided that the capacity of each subgrid is 20 kW. In p.u. domain, the voltage

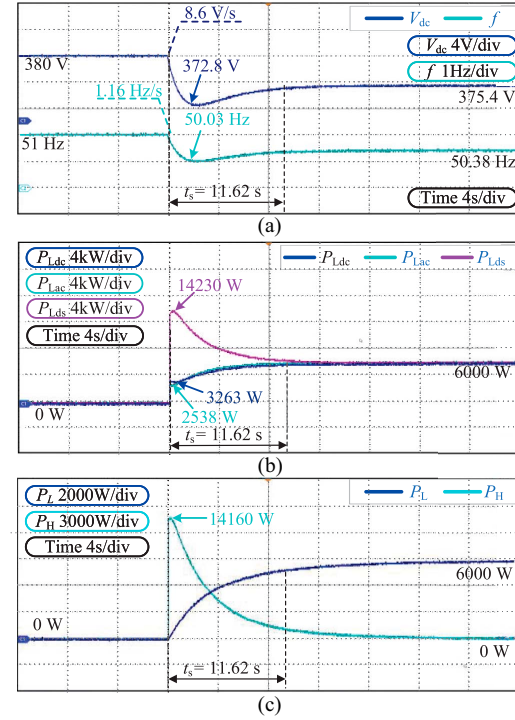


**Fig. 17.** Response process of hybrid ac/dc/DS when  $y_H = 30$ . (a) DC bus voltage and ac frequency response. (b) Output power of dc, ac, and DS subgrid. (c) Power allocation of ES<sub>L</sub> and ES<sub>H</sub> in DS subgrid.

drop across the impedance is  $0.0403 \times 0.3 = 0.012$  which is corresponding to the voltage drop of 4.6 V. This value is rightly equal to the voltage difference between two steady state points which are 380 and 375.4 V which justifies the correctness of both theoretical bode diagram in Fig. 11. Similar verification can be found in ac subgrid and DS subgrid.

In Fig. 16(a), the RoCoV, RoCoF, and settling time  $t_s$  are consistent with the result shown in Table I, which verifies that ECM can effectively evaluate the overall inertia of the system. Comparing Figs. 15(a) and 16(a), it can be observed that the RoCoV diminishes from 19.8 to 11.4 V/s at the onset of load fluctuations, while the minimum of the dc bus voltage exhibits an improvement from 368.5 to 372.2 V. Similar improvements also occur in the ac subgrid. The output power of each subgrid is shown in Fig. 16(b). It is noticeable that each subgrid compensates the load demand according to its own inertia in the transient state. In steady state, each subgrid outputs power proportional to its own capacity. The DS subgrid effectively participates in transient power regulation to improve the transient response of other subgrids. Fig. 16(c) illustrates the output power of the ES<sub>L</sub> and ES<sub>H</sub> in HESS, where ES<sub>L</sub> and ES<sub>H</sub> actively handle low frequency and high frequency power, respectively. When a step-up load change occurs, the ES<sub>H</sub> immediately responds to the rapid change in the load power and then gradually decreases to zero, while the output power of ES<sub>L</sub> slowly rises until it takes over all the load of the DS subgrid.

### C. Case 3

Fig. 17 shows the experimental results of the hybrid ac/dc/DS MG where  $y_H$  is increased to 30. The transient response of the

dc bus voltage and ac frequency are further optimized. The rate of change of the dc bus voltage at the onset of load perturbations is measured at 8.6 V/s, while the rate of change of frequency (RoCoF) is 1.16 Hz/s. Concurrently, the nadir point of dc bus voltage is recorded to 372.8 V, and the minimum frequency across the transient process is 50.03 Hz. In Fig. 17(b), it can be observed that the increase of  $y_H$  does not affect the static global power sharing. Regarding transient process, the transient power peak of ds subgrid rises to 14230 W, while the peak output power of dc and ac subgrids decreases relatively. Owing to the elevated transient power of the DS subgrid and the increase of  $y_H$ , the  $ES_H$  compensates for a greater proportion of the high-frequency components, whereas the  $ES_L$  exhibits a more gradual and stable output as shown in Fig. 17(c).

## V. CONCLUSION

This article presents a unified modeling for static and transient power regulation for hybrid ac/dc/DS microgrid (MG), delivering innovative insights into full-time-scale power control. The proposed model visualizes the power regulation process by representing the hybrid ac/dc/DS system as an equivalent circuit model (ECM). In addition, designing DS subgrid parameters with the help of ECM can optimize the power flow of the hybrid system and enhance the static and transient performance of the system. The traditional control coefficient in the  $ES_L$  is designed to achieve precise static global power sharing, while the inertia emulation loop in  $ES_H$  dynamically adjusts the transient power distribution. By strategically assigning the  $ES_L$  and  $ES_H$  with distinct response characteristics, the DS subgrid efficiently manages high and low frequency power, respectively, extending the life span of the HESS. The effectiveness and feasibility of the unified model are demonstrated through experimental results.

## REFERENCES

- [1] F. Blaabjerg, R. Teodorescu, M. Liserre, and A. Timbus, "Overview of control and grid synchronization for distributed power generation systems," *IEEE Trans. Ind. Electron.*, vol. 53, no. 5, pp. 1398–1409, Oct. 2006, doi: 10.1109/TIE.2006.881997.
- [2] C. Jin, P. Wang, J. Xiao, Y. Tang, and F. H. Choo, "Implementation of hierarchical control in dc microgrids," *IEEE Trans. Ind. Electron.*, vol. 61, no. 8, pp. 4032–4042, Aug. 2014, doi: 10.1109/TIE.2013.2286563.
- [3] F. Li , "An imbalance-status-enabled autonomous global power-sharing scheme for solid-state transformer interconnected hybrid ac/dc microgrids," *IEEE Trans. Smart Grid*, vol. 14, no. 3, pp. 1750–1762, May 2023, doi: 10.1109/TSG.2022.3216853.
- [4] P. C. Loh, D. Li, Y. K. Chai, and F. Blaabjerg, "Autonomous operation of hybrid microgrid with ac and dc subgrids," *IEEE Trans. Power Electron.*, vol. 28, no. 5, pp. 2214–2223, May 2013, doi: 10.1109/TPEL.2012.2214792.
- [5] P. C. Loh, D. Li, Y. K. Chai, and F. Blaabjerg, "Autonomous control of interlinking converter with energy storage in hybrid ac–dc microgrid," *IEEE Trans. Ind. Appl.*, vol. 49, no. 3, pp. 1374–1382, May/Jun. 2013, doi: 10.1109/TIA.2013.2252319.
- [6] P. Lin , "A distributed power management strategy for multi-paralleled bidirectional interlinking converters in hybrid ac/dc microgrids," *IEEE Trans. Smart Grid*, vol. 10, no. 5, pp. 5696–5711, Sep. 2019, doi: 10.1109/TSG.2018.2890420.
- [7] Q. Xu, J. Xiao, P. Wang, and C. Wen, "A decentralized control strategy for economic operation of autonomous ac, dc, and hybrid ac/dc microgrids," *IEEE Trans. Energy Convers.*, vol. 32, no. 4, pp. 1345–1355, Dec. 2017, doi: 10.1109/TEC.2017.2696979.
- [8] C. Sulzberger, "Triumph of AC. 2. The battle of the currents," *IEEE Power Energy Mag.*, vol. 1, no. 4, pp. 70–73, Jul./Aug. 2003.
- [9] D. Li, Q. Zhu, S. Lin, and X. Y. Bian, "A self-adaptive inertia and damping combination control of VSG to support frequency stability," *IEEE Trans. Energy Convers.*, vol. 32, no. 1, pp. 397–398, Mar. 2017, doi: 10.1109/TEC.2016.2623982.
- [10] A. Fathi, Q. Shafee, and H. Bevrani, "Robust frequency control of microgrids using an extended virtual synchronous generator," *IEEE Trans. Power Syst.*, vol. 33, no. 6, pp. 6289–6297, Nov. 2018, doi: 10.1109/TPWRS.2018.2850880.
- [11] A. Hosseiniour and H. Hojabri, "Virtual inertia control of PV systems for dynamic performance and damping enhancement of DC microgrids with constant power loads," *IET Renewable Power Gener.*, vol. 12, no. 4, pp. 430–438, 2018, doi: 10.1049/iet-rpg.2017.0468.
- [12] Z. Zhang, J. Fang, C. Dong, C. Jin, and Y. Tang, "Enhanced grid frequency and dc-link voltage regulation in hybrid ac/dc microgrids through bidirectional virtual inertia support," *IEEE Trans. Ind. Electron.*, vol. 70, no. 7, pp. 6931–6940, Jul. 2023, doi: 10.1109/TIE.2022.3203757.
- [13] J. Wang, W. Huang, N. Tai, M. Yu, R. Li, and Y. Zhang, "A bidirectional virtual inertia control strategy for the interconnected converter of standalone ac/dc hybrid microgrids," *IEEE Trans. Power Syst.*, vol. 39, no. 1, pp. 745–754, Jan. 2024, doi: 10.1109/TPWRS.2023.3246522.
- [14] Z. Zhang et al., "A modulated three-port interlinking converter for hybrid ac/dc/ds microgrids featured with a decentralized power management strategy," *IEEE Trans. Ind. Electron.*, vol. 68, no. 12, pp. 12430–12440, Dec. 2021, doi: 10.1109/TIE.2020.3040660.
- [15] P. Wang, C. Jin, D. Zhu, Y. Tang, P. C. Loh, and F. H. Choo, "Distributed control for autonomous operation of a three-port ac/dc/ds hybrid microgrid," *IEEE Trans. Ind. Electron.*, vol. 62, no. 2, pp. 1279–1290, Feb. 2015, doi: 10.1109/TIE.2014.2347913.
- [16] C. Jin, J. Wang, and P. Wang, "Coordinated secondary control for autonomous hybrid three-port ac/dc/ds microgrid," *CSEE J. Power Energy Syst.*, vol. 4, no. 1, pp. 1–10, Mar. 2018, doi: 10.17775/CSEEJPES.2016.01400.
- [17] B. Zakeri, G. C. Gissey, P. E. Dodds, and D. Subkhankulova, "Centralized vs. distributed energy storage—benefits for residential users," *Energy*, vol. 236, 2021, Art. no, doi: 121443, doi: 10.1016/j.energy.2021.121443.
- [18] P. Kundur, "Power system stability," *Power System Stability Control*, vol. 10, pp. 7–1, 2007.
- [19] P. Lin, P. Wang, J. Xiao, J. Wang, C. Jin, and Y. Tang, "An integral droop for transient power allocation and output impedance shaping of hybrid energy storage system in dc microgrid," *IEEE Trans. Power Electron.*, vol. 33, no. 7, pp. 6262–6277, Jul. 2018, doi: 10.1109/TPEL.2017.2741262.
- [20] J. Xiao, P. Wang, and L. Setyawan, "Multilevel energy management system for hybridization of energy storages in dc microgrids," *IEEE Trans. Smart Grid*, vol. 7, no. 2, pp. 847–856, Mar. 2016.
- [21] P. Lin et al., "A distributed control architecture for global system economic operation in autonomous hybrid ac/dc microgrids," *IEEE Trans. Smart Grid*, vol. 10, no. 3, pp. 2603–2617, May 2019, doi: 10.1109/TSG.2018.2805839.
- [22] J. Fang, H. Li, Y. Tang, and F. Blaabjerg, "Distributed power system virtual inertia implemented by grid-connected power converters," *IEEE Trans. Power Electron.*, vol. 33, no. 10, pp. 8488–8499, Oct. 2018, doi: 10.1109/TPEL.2017.2785218.
- [23] Q. Hong, M. A. U. Khan, C. Henderson, A. Egea-Àlvarez, D. Tzelepis, and C. Booth, "Addressing frequency control challenges in future low-inertia power systems: A great Britain perspective," *Engineering*, vol. 7, no. 8, pp. 1057–1063, 2021, doi: 10.1016/j.eng.2021.06.005.
- [24] W. Wu et al., "A virtual inertia control strategy for dc microgrids analogized with virtual synchronous machines," *IEEE Trans. Ind. Electron.*, vol. 64, no. 7, pp. 6005–6016, Jul. 2017, doi: 10.1109/TIE.2016.2645898.
- [25] C. Li, Y. Li, Y. Cao, H. Zhu, C. Rehtanz, and U. Häger, "Virtual synchronous generator control for damping dc-side resonance of VSC-MTDC system," *IEEE Trans. Emerg. Sel. Topics Power Electron.*, vol. 6, no. 3, pp. 1054–1064, Sep. 2018, doi: 10.1109/JESTPE.2018.2827361.
- [26] J. Fang, Y. Tang, H. Li, and X. Li, "A battery/ultracapacitor hybrid energy storage system for implementing the power management of virtual synchronous generators," *IEEE Trans. Power Electron.*, vol. 33, no. 4, pp. 2820–2824, Apr. 2018, doi: 10.1109/TPEL.2017.2759256.
- [27] A. Fathi, Q. Shafee, and H. Bevrani, "Robust frequency control of microgrids using an extended virtual synchronous generator," *IEEE Trans. Power Syst.*, vol. 33, no. 6, pp. 6289–6297, Nov. 2018, doi: 10.1109/TPWRS.2018.2850880.
- [28] S. Chen, Y. Sun, X. Hou, H. Han, S. Fu, and M. Su, "Quantitative parameters design of VSG oriented to transient synchronization stability," *IEEE Trans. Power Syst.*, vol. 38, no. 5, pp. 4978–4981, Sep. 2023, doi: 10.1109/TPWRS.2023.3293016.